

What Do Deep Neural Networks Find in Disordered Structures of Glasses?

Norihiro Oyama,^{1,*} Shihori Koyama,¹ and Takeshi Kawasaki²

¹*Toyota Central R&D Labs, Inc., Bunkyo-ku, Tokyo 112-0004, Japan*

²*Department of Physics, Nagoya University, Nagoya 464-8602, Japan*

(Dated: August 2, 2022)

Glass transitions are widely observed in a range of types of soft matter systems. However, the physical mechanism of these transitions remains unknown, despite years of ambitious research. In particular, an important unanswered question is whether the glass transition is accompanied by a divergence of the correlation lengths of the characteristic static structures. Recently, a method that can predict long-time dynamics from purely static information with high accuracy was proposed; however, even this method is not universal and does not work well for the Kob–Andersen system, which is a typical model of glass-forming liquids. In this study, we developed a method to extract the characteristic structures of glasses using machine learning or, specifically, a convolutional neural network. In particular, we extracted the characteristic structures by quantifying the grounds for the decisions made by the network. We considered two qualitatively different glass-forming binary systems and, through comparisons with several established structural indicators, we demonstrate that our system can identify characteristic structures that depend on the details of the systems. Surprisingly, the extracted structures were strongly correlated with the nonequilibrium aging dynamics on thermal fluctuation.

I. INTRODUCTION

When a liquid is cooled but crystallization is prevented by quenching or the addition of impurities, a liquid state can be maintained below the melting temperature, resulting in a so-called “supercooled” liquid state. The further cooling of the supercooled liquid results in a sudden increase in the viscosity of the liquid and yields a glass (more generally, an amorphous solid). In such a system, the particle motion is frozen, and the structure remains disordered. Various materials take on glassy states, for example, oxides, alloys, polymers, and colloids. Glassy materials are *generally* considered disordered and homogeneous because they cannot be distinguished from simple liquids that are also disordered in structure using analytical methods such as neutron, X-ray, or light scattering and other two-body correlations in the density field. However, dramatic changes to their properties can occur, for example, a 15-order-of-magnitude increase in the viscosity on a temperature change of only approximately 20%. Although the glass transition phenomenon has been studied for more than 150 years, its mechanism has not yet been clarified [1–5].

Heterogeneity in particle motion develops in supercooled liquids near the glass transition temperature, and the spatial length scale increases on such a glass transition [6, 7]. This behavior is called dynamic heterogeneity and is a potential cause of the rapid increase in viscosity at the glass transition point. However, to date, the origin of this dynamic heterogeneity has not been clarified; in particular, questions remain as to whether it is formed entirely dynamically or whether a static structure exists in the background. A theory that describes

the heterogeneity associated with glass transitions as a fully dynamic phenomenon is “dynamical facilitation theory,” and this theory explains the experimental results and numerical analysis of glass transitions [8]. On the other hand, “the theory of random first-order transition” (RFOT), which considers the glass transition as a thermodynamic phase transition and proposes a scenario in which a static conceptual structure called a “mosaic” develops, also explains the experimental results and numerical analysis of glass transitions [4, 9]. Accordingly, these various theories sometimes contradict each other, although both partially explain certain aspects of the glass transition phenomenon in a similar way. Therefore, no definitive theory for understanding glass transitions currently exists.

However, many attempts have been made to explore the specific structures that exist in supercooled liquids. For instance, icosahedral-like structures in metallic glasses [10, 11] and medium-range crystalline order in colloidal glasses with small particle-size dispersity have been found [12–14]. To extract these characteristic structures, order parameters are introduced on a system-by-system basis, but no order parameter applicable to *all* amorphous solids has been found. It is also unclear whether such characteristic structures are universal, and this is a topic of active debate. Therefore, elucidating the presence or absence of a universal structure in amorphous solids is a significant and challenging problem in fundamental physics. Tong and Tanaka recently developed a new order parameter consisting of the bond angles of particle structures and succeeded in extracting the characteristic structures correlated with particle dynamics for a wide range of glass-forming systems, including binary mixtures and polydisperse glassy systems with large particle size dispersions. However, as indicated in the corresponding literature [15, 16], this method has not been able to extract the characteristic structures in the Kob–

* Norihiro.Oyama.vb@mosk.tytlabs.co.jp

Andersen system [17], a typical glass-forming model, and, consequently, attempts to develop a universal structural analysis method for a variety of glass-like systems continues to the present day.

In recent years, machine-learning approaches have been widely used to investigate the characteristic structures governing glass dynamics [18, 19]. In particular, recent studies have successfully predicted the dynamics from the static structure in Kob–Andersen systems by learning from a large amount of structural data, as well as the corresponding dynamic data, using graph neural networks [20, 21]. However, although machine learning is very promising for exploring the structures of glasses, accurate learning is computationally expensive, and the results are difficult to interpret.

In this work, we propose a method to extract the characteristic multi-particle structures of glasses solely from the static configurations using a deep learning-based approach. To this end, we work on the classification problem for the random structures in glasses and liquids using a convolutional neural network (CNN) [22] and then identify the structures that the CNN relied on to make decisions using gradient-weighted class activation mapping (Grad-CAM) [23]. We applied our proposed method to two representative glass-forming liquid systems and compared the obtained structures with well-established structural indicators. The results demonstrate that the proposed method can extract qualitatively different characteristic structures in a system-detail-dependent manner. Astonishingly, although our method does not refer to information about the dynamics during the learning process and extracts the characteristic structure solely from the instantaneous static configurations, the obtained structures strongly correlate with the nonequilibrium aging dynamics.

The remainder of this paper is organized as follows. In Sec. II, we summarize the simulation methods and protocols used for sample preparation for the deep-learning tasks. In Sec. III, we introduce the CNN and Grad-CAM. We also provide a brief explanation of the established structural indicators used as a reference. In Sec. IV, the results of the structural analyses are presented, and the correlation between distinct indicators is discussed. The predictability of our method with respect to the dynamics is also discussed. Finally, in Sec. V, we provide a summary of this study and an overview of future research directions.

II. SIMULATIONS

A. System setups

In this study, we consider two distinct systems: the additive binary mixture (ABM) and the Kob–Andersen model (KAM) [17]. Both systems are two-dimensional (2D) and described by the Lennard–Jones (LJ) potential

with linear smoothing terms:

$$\phi_{ij}(r) = \phi_{ij}^*(r) - \phi_{ij}^*(r_{ij}^c) - (r - r_{ij}^c) \frac{d\phi_{ij}^*}{dr} \Big|_{r=r_{ij}^c}, \quad (1)$$

$$\phi_{ij}^*(r) = 4\epsilon_{ij} \left[\left(\frac{\sigma_{ij}}{r} \right)^{12} - \left(\frac{\sigma_{ij}}{r} \right)^6 \right], \quad (2)$$

where the subscript ij indicates that the variable is that between particles i and j , ϵ_{ij} sets the energy scale, σ_{ij} determines the interaction range, and r_{ij}^c is the cutoff length. The dynamics of the particles obey ϕ_{ij} , whereas ϕ_{ij}^* is the reference standard LJ potential. The smoothed LJ potential ϕ guarantees the continuity of the potential and force at cutoff distance $r = r_{ij}^c$, thus eliminating undesired artifact effects owing to the introduction of the cutoff [24].

Both systems are composed of two different types of particles (A and B) and are characterized by different parameters sets, such as ϵ_{ij} and σ_{ij} . In the case of the ABM, the parameters are simply additive; thus, we can unambiguously say that particle A is small and B is large (that is, $\sigma_{AA} = 5/6, \sigma_{AB} = 1, \sigma_{BB} = 7/6$, and ϵ_{ij} is unity) regardless of the combination of types of particles i and j . However, in the case of the KAM [17], the LJ parameters are nonadditive: $\sigma_{AA} = 1, \sigma_{AB} = 0.8, \sigma_{BB} = 0.88, \epsilon_{AA} = 1, \epsilon_{AB} = 0.5$, and $\epsilon_{BB} = 1.5$. Therefore, the concept of the “particle size” is not well defined in the KAM system.

All observables were nondimensionalized using characteristic length σ_c , characteristic energy ϵ_c , and particle mass m_c (the characteristic variables are listed in Table I). The nondimensionalized number density $\rho = N/L^2$ and number ratio of the two particle species also differ between the two systems, i.e., the ABM and KAM, although the total number of particles was fixed at $N = 2000$. With the values of ρ used here, the systems entered the glassy phase once the temperature was sufficiently low [17, 25]. Information about the parameters mentioned here is summarized in Table I.

B. Sample preparation protocol

We performed molecular dynamics (MD) simulations using the open-source Large-scale Atomic/Molecular Massively Parallel Simulator (LAMMPS: <https://www.lammps.org/>). We generated samples via NVT simulations using the Nosé–Hoover thermostat. Periodic boundary conditions were set in all directions. In this study, we aim to address a simple binary classification problem. For the two classes, we chose configurations at the temperature where the dynamic slowing-down starts at ($T_L = 2.0$ for the ABM and $T_L = 0.8$ for KAM) and at a very low temperature ($T_G = 0.05$ for both models). For both ABM and KAM, we first generated 5000 independent random configurations (4000 were used for training, 400 for validation, and 600 for the test data) and equilibrated them at a

TABLE I. Summary of model parameters

	m_A	m_B	σ_{AA}	σ_{AB}	σ_{BB}	ϵ_{AA}	ϵ_{AB}	ϵ_{BB}	N_A	N_B	ρ	σ_c	ϵ_c	m_c
ABM	1.0	1.0	5/6	1.0	7/6	1.0	1.0	1.0	1000	1000	1.2	σ_{AB}	ϵ_{AB}	m_A
KAM	1.0	1.0	1.0	0.8	0.88	1.0	0.5	1.5	700	1300	1.09	σ_{AA}	ϵ_{AA}	m_A

very high temperature of $T = 4.0$. The obtained configurations were then cooled at a constant cooling rate ($T \approx 8.33 \times 10^{-5}$), and the samples for the classification tasks were obtained at the desired temperatures T_L and T_G . The samples at T_L correspond to “equilibrium” supercooled liquids in the sense that their dynamics exhibit the time-translational invariance, whereas those at T_G are regarded as “nonequilibrium” glasses in the sense that they are expected to experience aging. Note that, judging from the evolution of the potential energy of the system as a function of the temperature (Fig. S2 in the Supplemental Material) [26], crystallization does not occur in either system at this cooling rate (i.e., we did not observe any discontinuous jumps in the energy). Consequently, if we measured the radial distribution function ($g(r)$) of the configurations at T_G , no signs of global crystallization were observed, although we did observe the development of a local organized structure (Fig. S3 in the Supplemental Material).

We stress that although we consider only 2D systems in this article for the sake of simplicity, all the analyses here can be easily extended to three-dimensional systems.

III. ANALYTICAL METHODS

A. Convolutional Neural Network (CNN)

In this work, we first perform classification using samples generated following the method described in Sec. II using a CNN [22, 27]. Obeying ref. [27] in which the authors tackled a similar classification task successfully, the network architecture had no pooling layers and is simply composed of three convolutional layers and subsequent activations (the rectified linear units), followed by the fully connected layer, dropout layer, and final fully connected layer as the output layer. Note that, although we apply the “softmax” function subsequently to obtain the final results, the output layer of the network is the fully connected layer to make it compatible with Grad-CAM, as explained in Sec. IIIB. The full details of the network and learning protocol, including the precise values of the hyperparameters, are summarized in the Supplemental Material. Importantly, when we feed the particle configurations, $\rho(\mathbf{r}) = \sum_i^N \delta(\mathbf{r} - \mathbf{r}_i)$, obtained from the MD simulations into the CNN, they are gridized by mapping operator \mathcal{M} : $\tilde{\rho} \equiv \mathcal{M}(\rho)$ (see Supplemental Material for technical details). Here, the tilde indicates that the variable is grid-based. We also mention that in the padding process at the convolutional layers, we use circu-

lar padding to consider the periodic boundary conditions properly.

B. Gradient-weighted class activation mapping (Grad-CAM)

The most significant feature of this work is the extraction of the characteristic mesoscale structures that the CNN relies on when classifying glasses and liquids. Such identification of the crucial information for the classification problem is called “class activation mapping” (CAM). The first-proposed simple CAM [28] assumed a global average pooling at the end of the network and, thus, cannot be utilized for networks with different types of architectures. This problem has been solved using a method called gradient-weighted class activation mapping (Grad-CAM) [23]. In Grad-CAM, CAM is calculated based on the differential of the output of the network with respect to the feature maps as

$$\alpha_m^C = \frac{1}{Z} \sum_k^u \sum_l^v \frac{\partial y^C}{\partial A_{k,l}^m}, \quad (3)$$

$$\tilde{L}^C = ReLU\left(\sum_m \alpha_m^C \tilde{A}^m\right), \quad (4)$$

where y^C is the score for class C ($C \in \{glass, liquid\}$ in the current setup) before softmax, \tilde{A}^m is the m -th feature map activation of a convolutional layer, $A_{k,l}^m$ is the (k, l) component of \tilde{A}^m , and $Z = uv$ is the normalizing factor for the global pooling calculation. The rectified linear unit $ReLU$ simply returns x if $x > 0$ and zero otherwise. In other words, in this Grad-CAM method, the characteristic part of the input information is identified as the weighted sum of the feature maps after a specified convolution layer (usually the last layer), and the weights are obtained depending on the global average of the sensitivity (gradient) of the output with respect to each pixel of the feature maps. Importantly, this method can be applied to networks with any architecture if the backpropagation is tractable.

The results presented in this paper are all particle-based Grad-CAM scores, $\Gamma = \sum_i^N \Gamma_i \delta(\mathbf{r} - \mathbf{r}_i)$, obtained using the inverse mapping operator \mathcal{M}^{-1} : $\Gamma \equiv \mathcal{M}^{-1}(\tilde{L}^C)$, where Γ_i is the Grad-CAM score of particle i . We simply call Γ the Grad-CAM score. Note that, hereinafter, all particle-based variables are coarse-grained and normalized (see the Supplemental Material for technical details, including the precise definition of Γ_i).

C. Voronoi volume

In this study, we compared the results of the proposed method with those of existing structural indicators to interpret the obtained Grad-CAM score, that is, Γ . The first reference indicator is the volume of the Voronoi cells Υ that particles reside in (here, we call them volumes, although they are in fact areas because the system is 2D).

The Voronoi cell to which particle i belongs can be uniquely defined without the introduction of any additional parameters, as follows:

$$V(\mathbf{r}_i) = \{\mathbf{r} | \mathcal{D}(\mathbf{r}, \mathbf{r}_i) \leq \mathcal{D}(\mathbf{r}, \mathbf{r}_j), j \neq i\}, \quad (5)$$

where $\mathcal{D}(\mathbf{a}, \mathbf{b})$ is a function that provides the 2D Euclidean distance between points \mathbf{a} and \mathbf{b} . The point \mathbf{r} in the equation is an arbitrary point in the system that is independent of the particle density field $\rho(\mathbf{r})$. The volume of the Voronoi cell for particle i can then be obtained as $\Upsilon_i \equiv \mathcal{V}(V(\mathbf{r}_i))$, where $\mathcal{V}(V)$ is the operator that gives the volume of region V . To achieve Voronoi tessellation, we used the *freud* [29, 30] Python library, which properly considers periodic boundary conditions. The Voronoi cell volumes provide a quantitative measure of the (inverse) local packing density. We call $\Upsilon = \sum_i^N \Upsilon_i \delta(\mathbf{r} - \mathbf{r}_i)$ the Voronoi volume.

D. Tong–Tanaka order parameter

Tong and Tanaka [15, 16] proposed an excellent order parameter that can quantify the dynamic properties of various types of glass-forming systems in terms of purely structural information in a unified manner. We call this order parameter the Tong–Tanaka order parameter (TT-OP). The TT-OP is undoubtedly the most successful structural indicator of the dynamic properties of glasses.

To calculate the TT-OP, we first look at each particle (e.g., particle o) and its neighbors (the particles sharing the edges of the Voronoi cell with center particle o). Then, particle o 's TT-OP, Θ_o , is obtained as the average difference between the angle formed by particle o and two of its neighbors that are adjacent to each other, θ_{ij}^1 , and the corresponding ideal angle θ_{ij}^2 (i.e., that realized when the distances between particles are exactly same as the sum of their ‘‘radii’’; see the Supplemental Material for more details and a schematic of the definitions of θ_{ij}^1 and θ_{ij}^2):

$$\Theta_o = \frac{1}{N_o} \sum_{\langle ij \rangle} |\theta_{ij}^1 - \theta_{ij}^2|, \quad (6)$$

where N_o is the number of particles neighboring particle o (this number agrees with the number of neighboring pairs of neighbors). The TT-OP $\Theta = \sum_i^N \Theta_i \delta(\mathbf{r} - \mathbf{r}_i)$ is defined as a particle-based indicator, and it has been proven that, for various systems, the spatially coarse-grained TT-OP

TABLE II. Classification accuracy for test data

ABM(G)	ABM(L)	KAM(G)	KAM(L)
1.00	1.00	1.00	0.998

predicts the dynamic propensity very correctly [16]. The results (not only of the TT-OP but also of all particle-based variables including the Grad-CAM score Γ) presented below are all spatially coarse-grained according to the method introduced in Ref. [16] with the coarse-graining length ξ fixed at $\xi = 3.0$ (and further normalized to the range $[0, 1]$; see the Supplemental Materials for technical details).

We again emphasize that TT-OP is undoubtedly the most successful purely structural predictor of the heterogeneous dynamics of various classes of glasses. However, even this indicator is not totally universal and is known to be inapplicable to the KAM, which is one of the most famous glass formers.

IV. RESULTS

A. Extraction of characteristic structures using Grad-CAM

The CNN introduced in Sec. III A was run over 250 epochs. During the training process, 4000 training data samples (for both glasses and liquids: 8000 samples in total) were provided with the correct labels indicating whether the samples were glasses or liquids. For both systems (ABM and KAM), the learning stage proceeded smoothly, and the classification accuracy reached almost 100% both for the training and validation data after this relatively small epochs. The same degree of the accuracy was achieved for the test data (the results for the test data are summarized in Table. II). We stress here that the calculation cost for the training part is very low in our setup: the entire 250 epochs of learning only took approximately 8 h using an NVIDIA Quadro P4000 (GP104GL).

Subsequently, using Grad-CAM, we further extracted the characteristic structures that the CNN relied on when identifying glass samples as *glasses*. Notably, this calculation requires only trivial cost (much less than a second for each sample). We present the typical results obtained for the ABM system in Fig. 1(a) and that of KAM in Fig. 2(a)). These results are both for the glass configurations: although we can also investigate the characteristic structures of liquids and, moreover, try to extract glass-like structures from liquids (and *vice versa*) within the Grad-CAM framework, in this study, we restricted ourselves to the investigation on the characteristic structures of glasses. Importantly, we discarded a sample for which the trained CNN gave the wrong classification (only 1 out of 2400 samples: in the case of the liquid in the KAM).

Although this sample could possess important information, we leave its investigation for future work.

B. Interpretable structural indicators

In the previous subsection, we showed that the CNN can correctly classify different random structures of glasses and liquids and visualize the characteristic structures that the CNN relies on to make decisions using Grad-CAM. In this section, we measure two distinct local multibody structural indicators to interpret the extracted structures. Because these indicators are handmade, we can take advantage of their interpretable nature. In the Supplemental Material, we present the two-body correlation function $g(r)$ for reference (Fig. S3).

We again stress that all the structural indicators, including the Grad-CAM score, were coarse-grained using the method introduced in Ref. [16] and further normalized to the interval $[0, 1]$. The coarse-grained length was chosen to be $\xi = 3.0$. See the Supplemental Material for technical details.

1. Voronoi volume

The Voronoi volume Υ is the first interpretable local multiparticle structural indicator. In this subsection, we briefly explain the obtained Υ values for the ABM and KAM systems. Fig. 1(b) presents the results for the ABM system, in which most particles exhibit relatively high values of Υ_i (> 0.4). The results for the KAM system are shown in Fig. 2(b), in which particles with small values of Υ_i (< 0.4) appear dominant.

These distinct trends are derived entirely from the difference in the set of interaction parameters (ϵ_{ij} and σ_{ij}) and the number ratio of the particle species (N_A/N_B). For instance, in the ABM system, because the area occupied by particles A is almost half that of particles B (the area fraction is 1 : 1.96), the region with a large Voronoi volume (corresponding to particles B) tends to be slightly dominant. In the KAM system, on the other hand, the interaction energy is most stable when different species are in contact, and the interaction range is also the shortest in this situation (see Table I). Therefore, small values of Υ_i are energetically favored in the KAM. Because samples with a very low temperature $T = 0.05$ are shown in Figs. 1 and 2, the structurally low-energy states are expected to be more probable. We also note that the small value of Υ_i does not necessarily mean that the local structure around particle i is highly ordered, as is evident in the case of the KAM.

2. Tong–Tanaka order parameter

The second interpretable structural indicator is the TT-OP Θ . As mentioned in Sec. IIID, of the various lo-

cally defined structural indicators reported to date, TT-OP captures the dynamical behavior of many classes of glasses most successfully. The characteristic structures of glasses in terms of the TT-OP are specified by small values of Θ_i , which means that the local structure is highly ordered. Because this is at odds with the definition of the Grad-CAM score Γ , we show $1 - \Theta$ instead of Θ so that the correspondence between the two is more easily understood. We stress that Θ is normalized to the interval $[0, 1]$ and, thus, is $1 - \Theta$.

The results for the ABM system are shown in Fig. 1(c). In contrast to the findings of Tong and Tanaka [15, 16], the structure is not well developed, and the spatial modulation is small: intermediate values are system-spanning. This is likely because our samples were generated by quenching at a fixed cooling rate and, thus, were not well annealed. We expect these samples to exhibit aging behavior.

The results for the KAM system are shown in Fig. 2(c). We note that because of the nonadditive nature of the potential parameters, defining a reference three-particle ideal configurational angle, θ^{\dagger} , in the case of the KAM is nontrivial. In this study, we employed the definition using the additive assumption ($\sigma_{AA} = 1.0$, $\sigma_{BB} = 0.88$, and $\sigma_{AB} = (\sigma_{AA} + \sigma_{BB})/2 = 0.94$) rather than the parameters used in the simulations because the reference structure is easier to interpret with this additive assumption. In this case, the spatial contrast becomes clearer than that of the ABM.

C. Correlations between different indicators

To interpret the Grad-CAM scores (Γ) obtained by our method, we further calculated the Pearson's correlation coefficients between different indicators for both the ABM and KAM. The results are summarized in Fig. 3. In this figure, we show violin plots of the coefficients between different indicators calculated using 600 samples for each case (ABM or KAM and glasses or liquids). Note that, when we calculated the correlation between TT-OP and other indicators, we used $1 - \Theta$ instead of Θ for consistency with the visualizations in Figs. 1(c) and 2(c).

We call the correlation coefficients between the Grad-CAM score and the Voronoi volume $C_{\Gamma, \Upsilon}$ and define those between different pairs in a similar manner: $C_{\Gamma, \Theta}$ and $C_{\Theta, \Upsilon}$. Although the results below are mostly those for the glass configurations only, we also mention the results for the liquids when we discuss their differences to those of the glass samples. Finally, we stress that, in the main text, all correlations are based on Pearson's definition. As presented in the Supplemental Material, however, we also obtained semi-quantitatively consistent results using Spearman's definition. In the following subsections, we explain the results for the ABM and KAM systems.

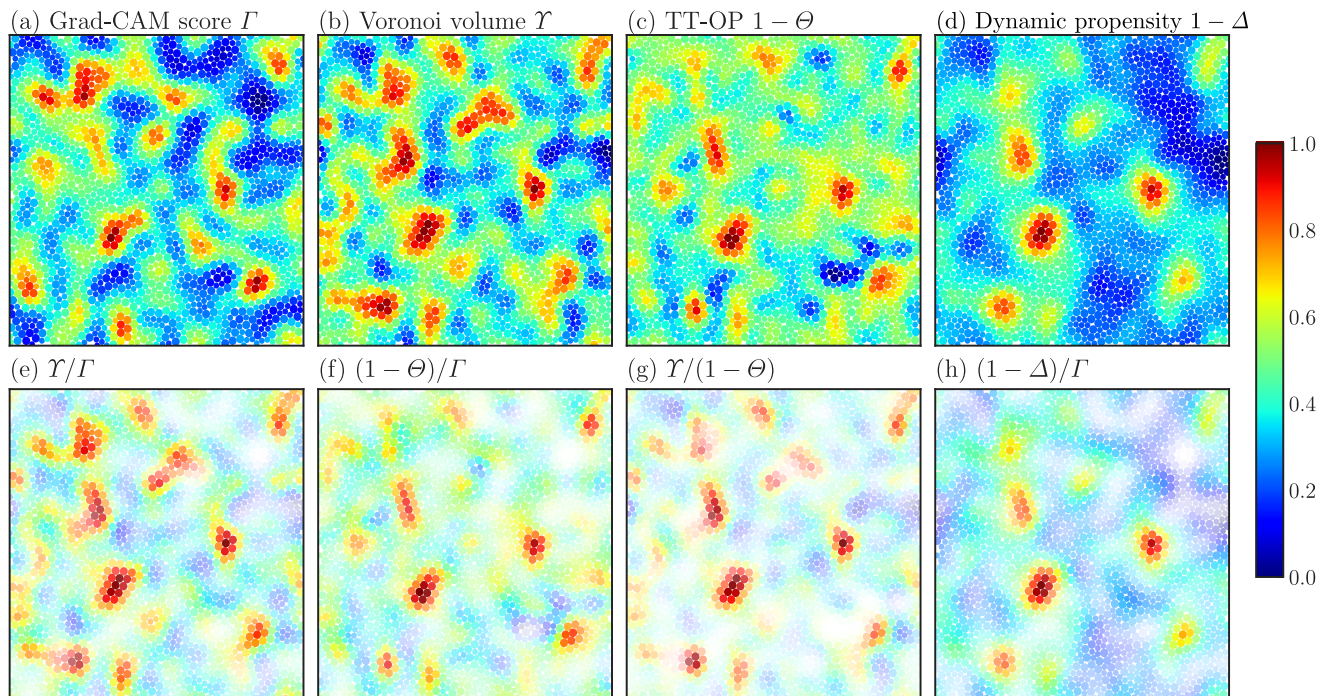


FIG. 1. Visualization of particle-based structural indicators for a typical glass configuration of the ABM system: (a) Grad-CAM score (Γ), (b) Voronoi volume (Υ), (c) TT-OP (Θ), (d) Dynamic propensity: Δ , and (d-f) visualizations of the indicators filtered by other indicators. In panels (d-f), the indicator shown on the left side of the titles are visualized with a filter that changes the value of the opacity to those of the indicator shown on the right side of the title. Because the spatial modulation of Θ is not large and, thus, simple filtering does not work well, Θ^2 is used as the opacity in the panel (g). Notice that all indicators are normalized to $[0,1]$, and the different colors distinguish the values as shown in the color bar. In addition, note that, in panels (c) and (d), $1 - \Theta$ and $1 - \Delta$ are shown rather than Θ and Δ for ease of comparison with the other indicators.

1. ABM

In the ABM system, $C_{\Gamma,\Upsilon}$ (the Grad-CAM score vs. the Voronoi volume) is the largest in terms of the intensity, and its average is an intermediate positive value: $\bar{C}_{\Gamma,\Upsilon}^G = 0.552$, where the bar represents the average over samples and the superscript G indicates that only the glass samples are considered (see the Supplemental Material for the summary of the average and the standard deviation of the correlation coefficients). This means that structures with large local volumes are judged to be characteristic of the glass. This behavior is consistent with the TT-OP: both $C_{\Gamma,\Theta}$ and $C_{\Theta,\Upsilon}$ (those for the Grad-CAM score vs. the TT-OP and the TT-OP vs. the Voronoi volume, respectively) are also positive despite the intensities being slightly smaller ($\bar{C}_{\Gamma,\Theta}^G = 0.403$ and $\bar{C}_{\Theta,\Upsilon}^G = 0.355$), meaning that structures with large values of the Voronoi volume tend to be more ordered (remember that the correlations with the TT-OP are calculated using $1 - \Theta$ and not Θ).

However, importantly, the difference between glasses and liquids is most evidently quantified by $C_{\Gamma,\Theta}$, which becomes completely positive for glasses but negative for liquids. On the other hand, the probability distribution of $C_{\Gamma,\Upsilon}$ shows a large overlap between glasses and liq-

uids; moreover, in the case of liquids, the distribution is bimodal, indicating that the Voronoi-volume-like aspect of the Grad-CAM score is likely unable to distinguish glasses and liquids accurately. Therefore, our method seems to rely on structures that are qualitatively consistent with the TT-OP rather than on the Voronoi volume when a decision is made, although Υ is closer to Γ than Θ in terms of the correlation for glass samples, as mentioned above ($\bar{C}_{\Gamma,\Upsilon}^G > \bar{C}_{\Gamma,\Theta}^G$). We stress that it has been proven that the TT-OP can extract the characteristic structures associated with the dynamics in binary additive glass formers [16] and our results are consistent with this.

2. KAM

Our method is further applicable to systems in which the interaction parameters are nonadditive and the definition of the TT-OP becomes ambiguous, such as the KAM system. In the case of the KAM system, unlike the results for the ABM, $C_{\Gamma,\Upsilon}$ and $C_{\Gamma,\Theta}$ for glasses are negative. Such a qualitative difference indicates that the structures extracted by our method respect the details of the systems. It should also be noted that, from the per-

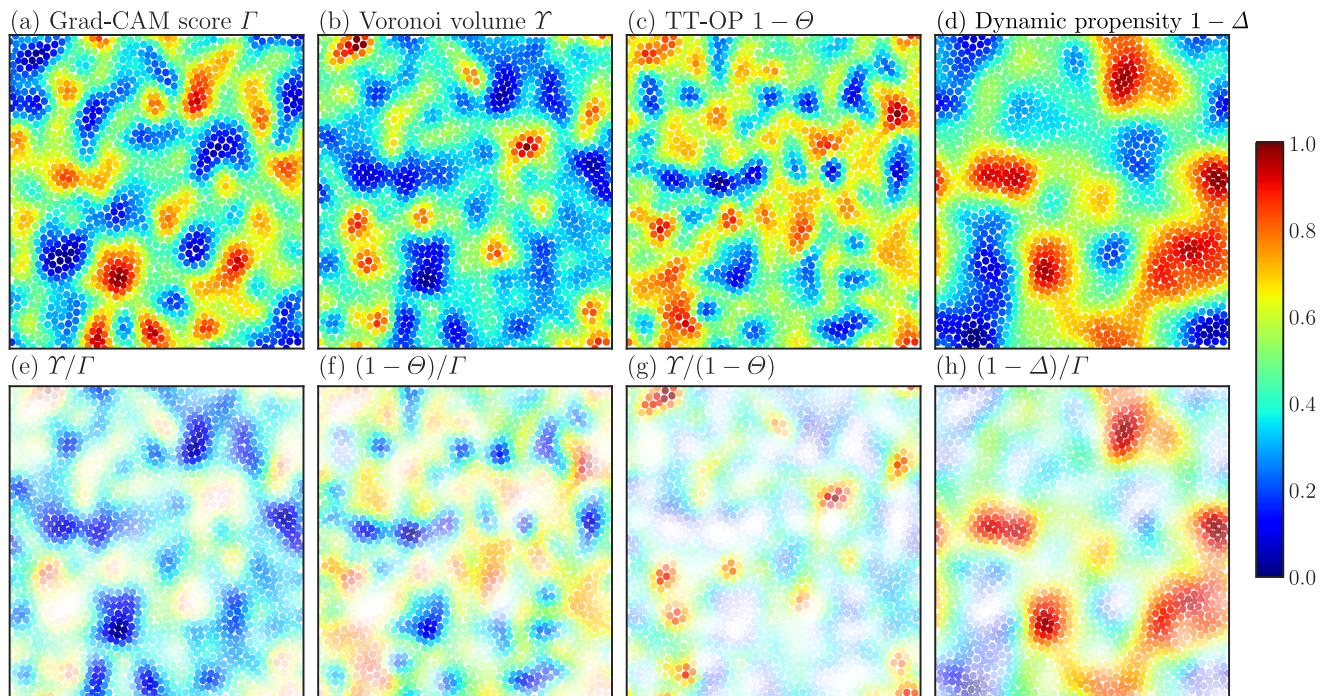


FIG. 2. Visualization of particle-based structural indicators for a typical glass configuration in the KAM system. The meanings of the panels are the same as those presented in Fig. 1.

spective of the intensity of the correlation coefficients, $C_{\Gamma, \Upsilon}$ is significantly larger than $C_{\Gamma, \Theta}$, and only $C_{\Gamma, \Upsilon}$ exhibits a clear difference in the signs between the results for glasses and liquids. This is another qualitative difference from the ABM system, where the difference in sign is evident for $C_{\Gamma, \Theta}$. However, although the TT-OP is a good descriptor for the ABM, as presented above, it is unlikely to characterize the properties of KAM systems. Thus, our method regards structures with high $C_{\Gamma, \Upsilon}$ as characteristic while $C_{\Gamma, \Theta}$ is small. In particular, the intensity of $C_{\Gamma, \Theta}$ is lower than that of $C_{\Theta, \Upsilon}$, suggesting that our method attempts to avoid correlation with the TT-OP selectively.

3. Wrap-up

To understand the behavior of the correlations between the different indicators presented above more intuitively, we present several special visualizations in Figs. 1(e-g) and 2(e-g), respectively. In these figures, one indicator (that shown on the left side of the panel titles) is shown in a filtered manner by setting another indicator (that shown on the right side) as opaque. That is, only red/blue areas are visible if the correlation is positive or negative (for example, Figs. 1(e-g) and 2(e)), and only random patterns are observed if the correlation is weak (Fig. 2(f)).

Interestingly, although we could interpret the Grad-CAM scores in terms of other conventional indicators

(the Voronoi volume and the TT-OP) to some extent in both the ABM and KAM, the correlations are not perfect and Grad-CAM seems to blend different indicators in an “appropriate” manner. In particular, we emphasize that the precise recipe of such blending is obviously dependent on the system details. Therefore, it would be meaningful to regress the obtained Grad-CAM score field Γ symbolically to achieve a fuller interpretation using recently invented methods [18, 31, 32].

D. Predictability of the dynamics

Thus far, we have shown that our method achieves the automatic extraction of characteristic glass structures in a tailor-made manner depending on the system details. Next, we asked the following question: Are the extracted structures correlated with some material properties, for example, the dynamics? To address this, we also investigate the so-called dynamic propensity [33–35] and compared the results with the Grad-CAM scores (Γ). Owing to the computational cost, we calculated the propensities only for the configurations shown in Figs. 1 and 2. For each configuration, we performed MD simulations with 30 different initial velocity distributions and calculated the so-called cage-relative squared displacement (CRSD), $\Delta_i^s(t)$, which is defined as $\Delta_i^s(t) = (\mathbf{d}_i^s(t) - \bar{\mathbf{d}}_i^s(t))^2$, where $\mathbf{d}_i^s(t) \equiv \mathbf{r}_i^s(t) - \mathbf{r}_i(0)$ is the displacement vector of the particle i at time t , $\bar{\mathbf{d}}_i^s \equiv \sum_j \mathbf{d}_j^s$ (the sum for

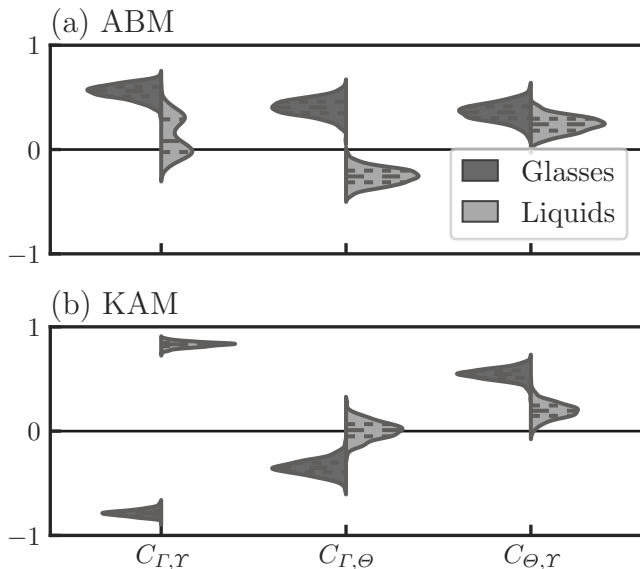


FIG. 3. Violin plots of the Pearson's correlation coefficients between distinct structural indicators. (a) Results for the ABM and (b) KAM systems. The dark gray parts represent the results for glasses and the light gray parts are for those of the liquids, as shown in the legend. The dashed lines indicate the quartiles.

j runs over the neighbors of i including i itself) is the average displacement vector of the cage to which particle i belongs, and the superscript s is the sample index (which distinguishes different realizations of the velocity distribution at $t = 0$). We stress that, because we considered an isoconfigurational ensemble, the initial configuration $\rho_0 = \sum_i^N \delta(\mathbf{r} - \mathbf{r}_i(0))$ does not depend on the samples. Then, the dynamic propensity Δ is defined as the average of the sample-dependent values of the CRSD, $\Delta^s = \sum_i^N \Delta_i^s \delta(\mathbf{r} - \mathbf{r}_i(0))$, over $N_s = 30$ samples as $\Delta \equiv \frac{1}{N_s} \sum_s^N \Delta^s$. Regarding the temperature during the measurement of the dynamics, we considered temperatures slightly above the glass transition point, T^* , (whose empirical definition is provided in the Supplemental Material; the obtained values are $T^* \approx 1.0$ for ABM and $T^* \approx 0.37$ for KAM) because we cannot expect any cage-breaking relaxational dynamics below T^* within the computationally accessible time window. To investigate the possible temperature dependence of the dynamics, we performed simulations at temperatures of up to approximately $1.5T^*$. We stress again that although the initial velocities follow the specified temperatures (which are higher than the glass transition point T^*), the initial configurations are drawn from the sample at $T_G = 0.05$ (those shown in Figs. 1 and 2).

The dynamic propensities in the ABM and KAM systems are shown in Figures 1(d) and 2(d), respectively. Because the characteristic structures of glasses are expected to be immobile, we visualized $1 - \Delta$, not Δ (remember that Δ is normalized to the interval $[0, 1]$), such

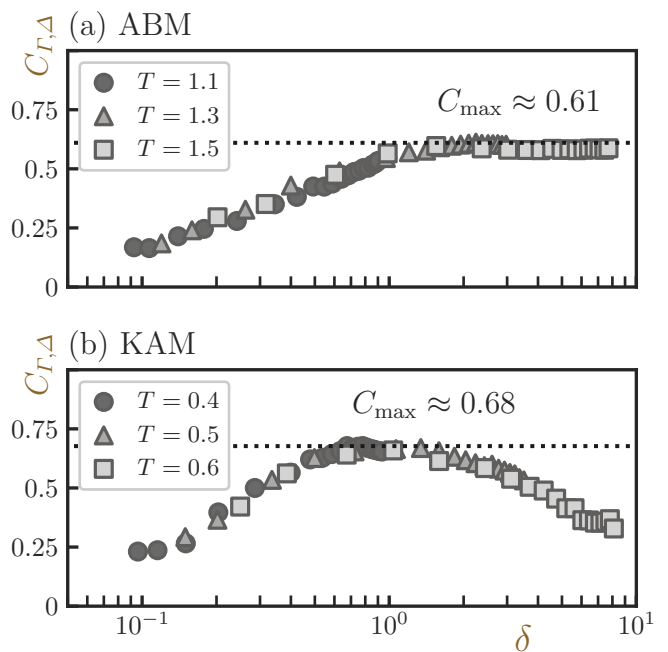


FIG. 4. The “time” evolution of the correlation between Grad-CAM score Γ and static propensity $1 - \Delta$ (see main text for the definition) as a function of the cage-relative route mean squared displacement δ . Each simulation was performed for 3×10^8 steps, and $\delta(t)$ during those simulations is plotted on the abscissa for each plot. Different markers are used to distinguish different temperatures as shown in the legend.

that the consistency with Γ is easier to perceive visually (in particular, we chose the propensity at the temperature and time that achieves the maximum correlation with Γ). Surprisingly, there is very good agreement between the spatial patterns of the Grad-CAM score (Γ) and static propensity ($1 - \Delta$) for both systems.

To quantify the correlation between Γ and Δ further, we calculated the Pearson's correlation coefficients, $C_{\Gamma,\Delta}$. The results are presented in Fig. 4 where the values for different temperatures are shown as functions of the cage-relative route mean-squared displacement. i.e., $\delta(t) = \frac{1}{N} \sum_i^N \sqrt{\Delta_i(t)}$. In this plot, the time dependence is indirectly reflected by the value of δ . Such a presentation allows us to compare the correlation between the dynamics (at different temperatures) and the static structure directly, thus ruling out the effect of the nontrivial dependence on time. Note that the correlation between Γ and $1 - \Delta$ is quantified, not Δ , in agreement with the visualization. From Fig. 4, we observe several striking consequences. First, $C_{\Gamma,\Delta}$ rises in accordance with the increase in δ , reaching its maximum value around $\delta \approx 1$ in both the ABM and KAM. This indicates that the structures extracted by our method are responsible for the α relaxation (note that these are nonequilibrium aging dynamics and not intra-metabasin equilibrium relaxation). Secondly, the change in the correlation $C_{\Gamma,\Delta}$ is nonmonotonic in the KAM system and it starts de-

creasing for $\delta \geq 1$, while it becomes plateau for $\delta \geq 1$ in the ABM system. These results indicate that the specified characteristic “well-ordered” clusters are transient in the KAM system whereas they seem very stable within the time window of our calculation in the ABM system. Thirdly, the maximum correlation, C_{\max} , reaches very high values in both systems: 0.61 and 0.68 in the ABM and KAM, respectively (see also Figs. 1(h) and 2(h), where the dynamic propensity fields $1 - \Delta$ filtered by the Grad-CAM scores are plotted; note that only low-mobility red parts survive). These incredibly strong correlations are comparable to those reported in Ref. [20] for which the characteristic structures were identified by the graph neural network, which uses information about the dynamics as a part of the training data input. This is surprising because our method does not require any information about the dynamics during the training process; thus, the computational cost for the training part is low. Finally, the results of different T follow a single master curve. This result confirms the fact that the dynamics are indeed governed by the static “glass structures,” at least in the temperature regime under study and concern nonequilibrium aging dynamics.

V. SUMMARY AND OVERVIEW

In this work, we proposed a method to extract the characteristic structures of amorphous systems solely from a couple of classes of static random configurations by means of classification with a CNN and quantification of the grounds for classification using Grad-CAM. We applied the proposed method to two qualitatively different binary glass-forming mixtures, the ABM and KAM, and showed that our method can automatically extract the system-detail-dependent mesoscopic characteristic structures of glasses. The proposed method has three outstanding features. First, our method can extract characteristic structures solely from the instantaneous static structures without any information about the dynamics. Secondly, the extracted characteristic structures are system-dependent; in other words, our method automatically identifies the tailor-made structural indicator suitable for each distinct system. Finally, the extracted structures are strongly correlated with the dynamic propensity, and the correlation coefficient is as high as that in the report of the state-of-the-art method [20]. The time evolution of the correlation reveals that the characteristic structure is closely related to the dynamics corresponding to the so-called α relaxation, where the mean route cage-relative squared dis-

placement is of the order of unity: $\delta \approx 1$. Moreover, such a correlation is robust over a wide range of temperatures, at least in the range $T^* \leq T \leq 1.5T^*$. We again stress that, unlike in previously reported studies, our dynamic propensity quantifies the nonequilibrium aging processes not the intra-metabasin equilibrium relaxational dynamics.

Finally, we discuss several future research directions. First, we should conduct a similar analysis using well-annealed glass configurations because the equilibrium dynamics are important to understand the properties of glasses more deeply. In particular, it is challenging to determine whether the characteristic structures that our method extracts for equilibrium glass configurations are correlated with the equilibrium dynamics. Moreover, our method can find the characteristic structures from the static configurations alone, even when the microscopic physical quantity that characterizes the two classes (e.g., the dynamic propensity) is not available, as long as the two different classes are defined, for example, by specifying macroscopic quantities, such as the temperature. Therefore, it allows us to directly ask, for example, whether we observe any structural differences between normal glasses and ultrastable glasses [36, 37] for which the dynamical properties are numerically intractable. Because ref. [38] reported that the stability of glass samples is structurally reflected by the density of the quasi-localized vibrational (QLV) modes, it would be very interesting to see if Grad-CAM also quantifies the QLV modes or highlights completely different structures. Similarly, it has been shown that the structural difference between instantaneous configurations under different external shear speeds is quantified by the density of the imaginary normal modes [39]. Our method is also applicable in such situations.

In general, we expect that the extracted structures are dependent on the precise setup of the classification problem, such as the temperature choice for each class. It would be interesting to compare the characteristic glass structures obtained from different reference high temperatures. Further, such structures could be sensitive to the details of the protocols, for example, the network architecture or number of epochs. The length scale ξ used for the coarse-graining of structural indicators also warrants further consideration, and the investigation of the effects of these factors would be valuable.

The authors thank Satoshi Koide and Takenobu Nakamura for fruitful discussions. This work was financially supported by the JST FOREST Program (Grant No. JPMJFR212T) and JSPS KAKENHI (Grant Nos. 22H04472, 20H05157, 20H00128, 19K03767, 18H01188).

[1] C. A. Angell, Formation of Glasses from Liquids and Biopolymers, *Science* (80-.). **267**, 1924 (1995).
 [2] P. G. Debenedetti and F. H. Stillinger, Supercooled liquids and the glass transition, *Nature* **410**, 259 (2001).

[3] J. C. Dyre, Colloquium : The glass transition and elastic models of glass-forming liquids, *Rev. Mod. Phys.* **78**, 953 (2006).
 [4] A. Cavagna, Supercooled liquids for pedestrians, *Physics*

- Reports **476**, 51 (2009).
- [5] L. Berthier and G. Biroli, Theoretical perspective on the glass transition and amorphous materials, *Rev. Mod. Phys.* **83**, 587 (2011).
 - [6] R. Yamamoto and A. Onuki, Dynamics of highly supercooled liquids: Heterogeneity, rheology, and diffusion, *Physical Review E* **58**, 3515 (1998).
 - [7] R. Yamamoto and A. Onuki, Heterogeneous Diffusion in Highly Supercooled Liquids, *Physical Review Letters* **81**, 4915 (1998).
 - [8] D. Chandler and J. P. Garrahan, Dynamics on the Way to Forming Glass: Bubbles in Space-Time, *Annual Review of Physical Chemistry* **61**, 191 (2010).
 - [9] T. R. Kirkpatrick, D. Thirumalai, and P. G. Wolynes, Scaling concepts for the dynamics of viscous liquids near an ideal glassy state, *Physical Review A* **40**, 1045 (1989).
 - [10] A. Hirata, P. Guan, T. Fujita, Y. Hirotsu, A. Inoue, A. R. Yavari, T. Sakurai, and M. Chen, Direct observation of local atomic order in a metallic glass, *Nature Materials* **10**, 28 (2011).
 - [11] A. Hirata, L. J. Kang, T. Fujita, B. Klumov, K. Matsue, M. Kotani, A. R. Yavari, and M. W. Chen, Geometric Frustration of Icosahedron in Metallic Glasses, *Science* **341**, 376 (2013).
 - [12] T. Kawasaki, T. Araki, and H. Tanaka, Correlation between Dynamic Heterogeneity and Medium-Range Order in Two-Dimensional Glass-Forming Liquids, *Physical Review Letters* **99**, 215701 (2007).
 - [13] H. Tanaka, T. Kawasaki, H. Shintani, and K. Watanabe, Critical-like behaviour of glass-forming liquids, *Nature Materials* **9**, 324 (2010).
 - [14] M. Leocmach and H. Tanaka, Roles of icosahedral and crystal-like order in the hard spheres glass transition, *Nature Communications* **3**, 974 (2012).
 - [15] H. Tong and H. Tanaka, Revealing Hidden Structural Order Controlling Both Fast and Slow Glassy Dynamics in Supercooled Liquids, *Physical Review X* **8**, 011041 (2018).
 - [16] H. Tong and H. Tanaka, Structural order as a genuine control parameter of dynamics in simple glass formers, *Nature Communications* **10**, 5596 (2019).
 - [17] W. Kob and H. C. Andersen, Testing mode-coupling theory for a supercooled binary Lennard-Jones mixture. II. Intermediate scattering function and dynamic susceptibility, *Physical Review E* **52**, 4134 (1995).
 - [18] S. S. Schoenholz, E. D. Cubuk, E. Kaxiras, and A. J. Liu, Relationship between local structure and relaxation in out-of-equilibrium glassy systems, *Proceedings of the National Academy of Sciences* **114**, 263 (2017).
 - [19] E. Boattini, S. Marín-Aguilar, S. Mitra, G. Foffi, F. Smalenburg, and L. Filion, Autonomously revealing hidden local structures in supercooled liquids, *Nature Communications* **11**, 5479 (2020).
 - [20] V. Bapst, T. Keck, A. Grabska-Barwińska, C. Donner, E. D. Cubuk, S. S. Schoenholz, A. Obika, A. W. R. Nelson, T. Back, D. Hassabis, and P. Kohli, Unveiling the predictive power of static structure in glassy systems, *Nature Physics* **16**, 448 (2020).
 - [21] S. Hayato, H. Masatoshi, S. Toyotaro, and S. Takashi, Unraveling intricate processes of glassy dynamics from static structure by machine learning relative motion, [arxiv:2206.14024](https://arxiv.org/abs/2206.14024) doi.org/10.48550/arXiv.2206.14024, [arXiv:2206.14024](https://arxiv.org/abs/2206.14024).
 - [22] M. Valueva, N. Nagornov, P. Lyakhov, G. Valuev, and N. Chervyakov, Application of the residue number system to reduce hardware costs of the convolutional neural network implementation, *Mathematics and Computers in Simulation* **177**, 232 (2020).
 - [23] R. R. Selvaraju, M. Cogswell, A. Das, R. Vedantam, D. Parikh, and D. Batra, Grad-CAM: Visual Explanations from Deep Networks via Gradient-Based Localization, *International Journal of Computer Vision* **128**, 336 (2020).
 - [24] M. Shimada, H. Mizuno, and A. Ikeda, Anomalous vibrational properties in the continuum limit of glasses, *Physical Review E* **97**, 022609 (2018).
 - [25] N. Oyama, H. Mizuno, and A. Ikeda, Unified view of avalanche criticality in sheared glasses, *Physical Review E* **104**, 015002 (2021).
 - [26] S. Sastry, P. G. Debenedetti, and F. H. Stillinger, Signatures of distinct dynamical regimes in the energy landscape of a glass-forming liquid, *Nature* **393**, 554 (1998).
 - [27] K. Swanson, S. Trivedi, J. Lequieu, K. Swanson, and R. Kondor, Deep learning for automated classification and characterization of amorphous materials, *Soft Matter* **16**, 435 (2020).
 - [28] B. Zhou, A. Khosla, A. Lapedriza, A. Oliva, and A. Torralba, Learning Deep Features for Discriminative Localization, in *2016 IEEE Conference on Computer Vision and Pattern Recognition (CVPR)* (IEEE, 2016) pp. 2921–2929.
 - [29] V. Ramasubramani, B. D. Dice, E. S. Harper, M. P. Spellings, J. A. Anderson, and S. C. Glotzer, *freud*: A software suite for high throughput analysis of particle simulation data, *Computer Physics Communications* **254**, 107275 (2020).
 - [30] B. Dice, V. Ramasubramani, E. Harper, M. Spellings, J. Anderson, and S. Glotzer, Analyzing Particle Systems for Machine Learning and Data Visualization with *freud* (2019) pp. 27–33.
 - [31] S. L. Brunton, J. L. Proctor, and J. N. Kutz, Discovering governing equations from data by sparse identification of nonlinear dynamical systems, *Proc. Natl. Acad. Sci.* **113**, 3932 (2016).
 - [32] S. H. Rudy, S. L. Brunton, J. L. Proctor, and J. N. Kutz, Data-driven discovery of partial differential equations, *Sci. Adv.* **3**, 10.1126/sciadv.1602614 (2017).
 - [33] A. Widmer-Cooper, P. Harrowell, and H. Fynewever, How Reproducible Are Dynamic Heterogeneities in a Supercooled Liquid?, *Phys. Rev. Lett.* **93**, 135701 (2004).
 - [34] A. Widmer-Cooper and P. Harrowell, On the study of collective dynamics in supercooled liquids through the statistics of the isoconfigurational ensemble, *The Journal of Chemical Physics* **126**, 154503 (2007).
 - [35] L. Berthier and R. L. Jack, Structure and dynamics of glass formers: Predictability at large length scales, *Physical Review E* **76**, 041509 (2007).
 - [36] L. Berthier, P. Charbonneau, E. Flenner, and F. Zamponi, Origin of Ultrastability in Vapor-Deposited Glasses, *Physical Review Letters* **119**, 188002 (2017).
 - [37] D. Khomenko, C. Scalliet, L. Berthier, D. R. Reichman, and F. Zamponi, Depletion of Two-Level Systems in Ultrastable Computer-Generated Glasses, *Physical Review Letters* **124**, 225901 (2020).
 - [38] L. Wang, A. Ninarello, P. Guan, L. Berthier, G. Szamel, and E. Flenner, Low-frequency vibrational modes of stable glasses, *Nature Communications* **10**, 26 (2019).
 - [39] N. Oyama, H. Mizuno, and A. Ikeda, Instantaneous Nor-

mal Modes Reveal Structural Signatures for the Herschel-

Bulkley Rheology in Sheared Glasses, Physical Review Letters **127**, 108003 (2021).